Considering microtexture geometry to improve micro-injection molding fidelity

Damon G.K. Aboud[1], Nicole Demarquette[2], Denis Rodrigue[3], Anne-Marie Kietzig[1]*

[1] Department of Chemical Engineering, McGill University, Montreal, Quebec, Canada
[2] Department of Mechanical Engineering, Ecole de Technologie Supérieure, Montréal, Québec, Canada
[3] Department of Chemical Engineering, Laval University, Québec, Canada

*Corresponding author: anne.kietzig@mcgill.ca

Keywords: micro–injection molding, injection molding, laser machining, polymer flow, mold design, micro/nanostructure, processing conditions.

Highlights:

- Micro-injection molding of hierarchical geometric pillar arrays
- Compared different geometric patterns of microstructure arrays
- Novel analytical method: roughness comparison of hierarchical microbumps
- Triangular geometric arrays outperform squares, hexagons, and rhombuses
- Air drainage through geometric valleys is major determinant of replication quality

Abstract

Micro-injection molding (μIM) is an attractive manufacturing technique to produce microstructured parts at low cost and high throughput. However, due to the small feature sizes to be molded, μIM presents unique engineering challenges to overcome. Accordingly, extensive research has focused on improving the mold design and molding parameters in order to improve the limitations and ultimately the replication fidelity of the process. In this report, we investigate one variable that has not yet been considered: the microstructure's geometric pattern. Hence, we used laser micromachining techniques to inscribe geometric arrays of hierarchical micropillars in the shapes of squares, rhombuses, hexagons, and triangles. By developing a novel analysis protocol based on the roughness of "microbumps" transferred from the mold to the replicates, our results demonstrate that triangular and hexagonal microstructure arrays lead to higher replication fidelity due to their improved air drainage properties compared to the other geometries tested. In addition, to put the geometry's influence into a broader perspective, we also tested several molding parameters including the holding pressure, melt temperature, mold temperature, and choice of polymer resin. We found that the use of high holding pressure is most strongly correlated with high replication fidelity, whereas the temperature and resin variables had a relatively small impact on our molding process.

1 Introduction

Because injection molding (IM) is a low cost, high throughput, and scalable manufacturing method, it is used to produce plastic parts intended for a wide variety of industries and products. In recent years, research has focused on micro-injection molding (μIM), which is often separated into three distinct categories: (I) molding of small parts with a mass on the milligram scale, (II) large parts whose

size tolerance is on the micrometer scale, and (III) large parts containing detailed regions of microfeatures [1]. This study focuses on advancing knowledge of category III (also known as "micro-to-macro" structures [2]), for which other studies already explored a wide range of potential applications including superhydrophobic surfaces [3-6], medical diagnostic technology [2], diffractive optical gratings [7-9], antireflective surfaces [10-12], microfluidic devices [13-15], and functional substrates for cell cultures [16-19].

Compared to conventional (macro-scale) polymer injection molding, μIM presents several unique engineering challenges. For example, during conventional injection molding, the molten polymer typically exhibits laminar flow through the mold cavity, whereas during μIM, instabilities may arise in the melt flow due to rapid changes in geometry, thin cavity sections, or the presence of gates [20]. In addition, the "wall slip" effect occurs during μIM when the shear stress at the polymer/mold interface is high, prompting the melt to slip along the mold wall instead of conforming to the theoretical no-slip boundary condition [21]. This effect is often magnified in μIM due to the mold's thinner cavities and textured surfaces, which promotes higher shear stress, more wall slip, and higher melt flow instability [20-22]. Furthermore, micro-textures on the mold's surface increase the surface area, which promotes higher demolding forces. This can cause stress marks, deformation fracture, and stretching of the microstructures during demolding [23].

Another significant challenge of μIM is the "hesitation effect", which occurs because the injected polymer preferentially fills the largest cavities of the mold first, until the cavity pressure increases enough to overcome the flow resistance of the microstructures, at which point the melt can finally be driven into the microscopic cavities [24-26]. This causes the melt to hesitate at the entrance of the microstructures, during which it may begin to solidify into a skin layer, increasing its viscosity and preventing complete filling of the microcavities. As a result, the polymer often solidifies before

reaching the deepest valleys of the topographical structure of the mold, resulting in truncated microstructures on the polymer replicate [27, 28]. This is especially true for microstructures with high aspect ratios, since deeper cavities have more surface area and take longer to fill [29]. Previous studies have recommended applying rapid heat cycling or Variotherm technology to overcome the hesitation effect [2, 30].

Finally, effective air drainage solutions are especially important for μIM since the complex microstructured topographies present on the mold's surface are more prone to retaining air pockets than the smooth walls present in most conventional molding processes. Hence, while conventional IM relies on air vents built into the mold, μIM often requires an evacuation system (venting) [2, 31]. Effective drainage is important to prevent air pockets from becoming trapped between the mold and polymer, or between converging flow fronts. This can result in burn marks or "short shots", where the plastic does not fill the entire mold. In extreme cases where the trapped gas is compressed to excessively high pressures, air pockets can result in the diesel effect, resulting in combustion [32].

Previous studies on μIM have focused on many novel solutions to overcome the unique challenges listed above and improve the replication fidelity. For example, Zhou et al. applied a fluoroalkyl silane (FAS) low-adhesion coating to their mold. This approach successfully reduced the mold/resin adhesion forces, resulting in high-aspect ratio nanopillars that were not achievable on the uncoated mold [28]. Liparoti et al. applied a thin, carbon black loaded poly(amide-imide) heating plane to achieve rapid heat cycling (RHC) via the Joule effect. This innovation led to greatly increased heating and cooling rates (up to 50 K/s), allowing for faster part replication and a reduction in the required injection pressure of their μIM process [33]. Su et al. performed a parametric study of μIM parameters including both numerical and experimental results. Although elevated melt temperature was the most important factor to reduce the presence of voids in the finished parts, air evacuation was also critically

important [31]. Zhou et al. performed a careful study of the crystalline properties of polyoxymethylene to determine how the ratio between the crystallization time and chain relaxation time affect the final polymer structure. They found that, due to the fast cooling and high shear rates involved in μIM, the resin near the mold walls (where the cooling rate is highest) is prone to generating a semi-crystalline structure, whereas the resin in the core of the molded part (where crystallization time is longer) tends to recover a random coil state [34]. Wang et al. fabricated a composite mold insert composed of nickel with WS_2 nanoparticles, to reduce part deformation during demolding. They found that the resulting mold surface led to a 66% reduction in friction forces and better replication fidelity of micro-injection molded PMMA sensors [35].

In this report, we focus on an often-overlooked factor: the geometric pattern of the mold's microstructure, which is a topic that has not yet been considered by other researchers in the field. Hence, we inscribed arrays of square, hexagonal, rhombic, and triangular micropillars on the mold. By micro-injection molding these patterns using two different resins at various holding pressures, mold temperatures, and melt temperatures, we assess how these different patterns influence the replication fidelity of the finished part. Since this study focuses on Category III μIM (macro-scale parts decorated with microstructures), this work is intended to guide mold design choices for industrial scale manufacturing of functionalized products.

2 Methods

2.1 Characterization Methods

Scanning electron microscopy (SEM) images were acquired using an FEI Inspect F50 electron microscope. Confocal microscope images and data were acquired using an Olympus LEXT OLS5000 laser scanning confocal microscope.

The analysis focuses heavily on comparing the areal roughness values of microstructures on the molded parts. To accomplish this task, the Olympus OLS5000 Analysis Application was used to export topographical data from the confocal microscope images, which were then analyzed using a custom MATLAB code. The MATLAB code measures the areal roughness (S_a) of specific regions of interest (ROI) for each structure, according to the arithmetical mean height definition:

$$S_a = \frac{1}{A}\iint_A |z(x,y)|\, dx\, dy \qquad \text{Equation 1}$$

in which A is the measurement area, and $z(x,y)$ is the height (z) deviation at position (x,y) from the mean z-value of the surrounding topography. This analysis approach is explained at greater length in **Supporting Note 1**, which specifies the exact region of interest for each geometric pattern.

For each experimental setting, 5 micro-injection molded samples were produced for analysis. Accordingly, most measurements presented in this report represent the average of 5 individual measurements. However, due to some damage occurring to samples during shipping, some data points are comprised of only 3 or 4 measurements (as indicated by the empty boxes in **Tables S1-4** in **Supporting Note 2**). All error bars and margins of error in this report represent two standard deviations of the dataset.

2.2 Mold Insert Fabrication

Test areas (subsequently called patches) of geometric microstructures were fabricated via femtosecond laser micromachining on a mold insert. The mold insert is a $1.50 \times 1.62 \times 1.35$ cm^3 block of P20 tooling steel and is depicted in **Figure 1(a)**, which presents a flowchart of our experimental process. The mold insert was positioned and scanned under the laser beam using a 3D translation platform purchased from Newport Corporation (Irvine, CA, United States). The system consists of two XMS50-S linear translation stages representing the x- and y-axes, and an MVN80 vertical linear stage allowing for z-axis movement. A Newport XPS universal high-performance motion/driver controller was used to drive the stage setup, using custom made PVT (position-velocity-time) trajectory codes to inscribe the desired microstructures. The laser was a Carbide CB3, 40 W pulsed laser (Light Conversion) with a central wavelength of $\lambda = 1030$ nm. The pulse energy was 200 μJ, the pulse repetition rate was 2.5 kHz, and the pulse duration was approximately 250 fs. The beam was focused using a bi-convex lens with a focal length of 10 cm, resulting in a theoretical spot radius of 13.6 μm and a pulse peak fluence of 66.4 J/cm^2. The raster scanning speed was 10 mm/s (corresponding to 6.8 pulses per spot), and the spacing between adjacent scan lines was 4 μm. Each patch was scanned either 12 or 13 times to reach the desired ablation depth.

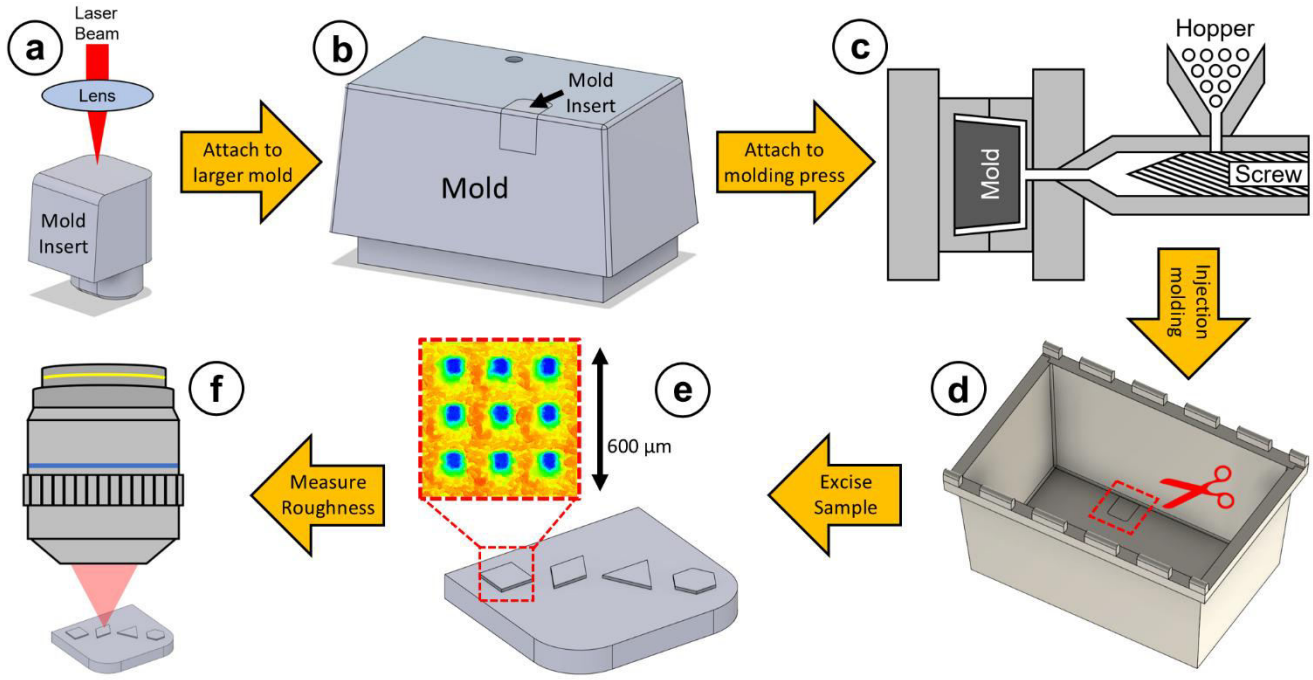

Figure 1. Flow chart of the experimental method: (a) A small steel mold insert ($\mathbf{1.50 \times 1.62 \times 1.35}$ cm^{3}) is laser micromachined to inscribe patches of geometric micropillars. (b) The mold insert is attached to a larger steel mold that defines the interior shape of a rectangular pail ($\mathbf{12.3 \times 8.1 \times 6.3}$ cm^{3}). (c) Injection molding is performed by attaching the mold assembly to a Toshiba 90A injection molding machine. The molding parameters are varied according to **Table 2**. (d) A small rectangular sample is cut from the larger pail at the location corresponding to the mold insert's position. (e) Schematic representation of an excised sample. The inset displays a confocal microscope image of a square pattern replicated on the polymer. (f) The roughness of the secondary microbumps that decorate the replicated primary geometric cavity arrays is measured via confocal microscopy.

Figure 2(a) provides scanning electron micrographs of each microstructured patch inscribed on the mold insert. In addition, **Figure 2(b)** shows confocal microscope heatmaps, in which warm colours (such as red) indicate topographical peaks, and cool colours (such as blue) indicate valleys. As a result of the laser processing parameters, dual-scale hierarchical microstructures were fabricated. Specifically, in the valleys between the primary geometric pillar arrays (with length scales in the 100 µm range), a hierarchical substructure of microholes (with length scales in the 10 µm range) developed. For clarity,

the coloured arrows in **Figure 2(a)** identify the difference between the primary geometric pillar array (1-GPA) and the secondary microholes (2-MH), and **Figure 2(d)** (corresponding to the red box indicated in **Figure 2(a)**) shows a high magnification image of the secondary microholes. The microholes are consistent with the "holes" microstructures defined by Ahmmed et al. (2014), who noted that the microholes are not formed by the drilling action of individual laser pulses, but instead through a complex physical mechanism that develops throughout the raster scanning process [37]. This dual-scale hierarchical structure was selected as the basis for this study because the molded replicates are representative of functional microstructures developed for applications in fields such as superwetting surfaces [38, 39] and cell adhesion/migration studies [40].

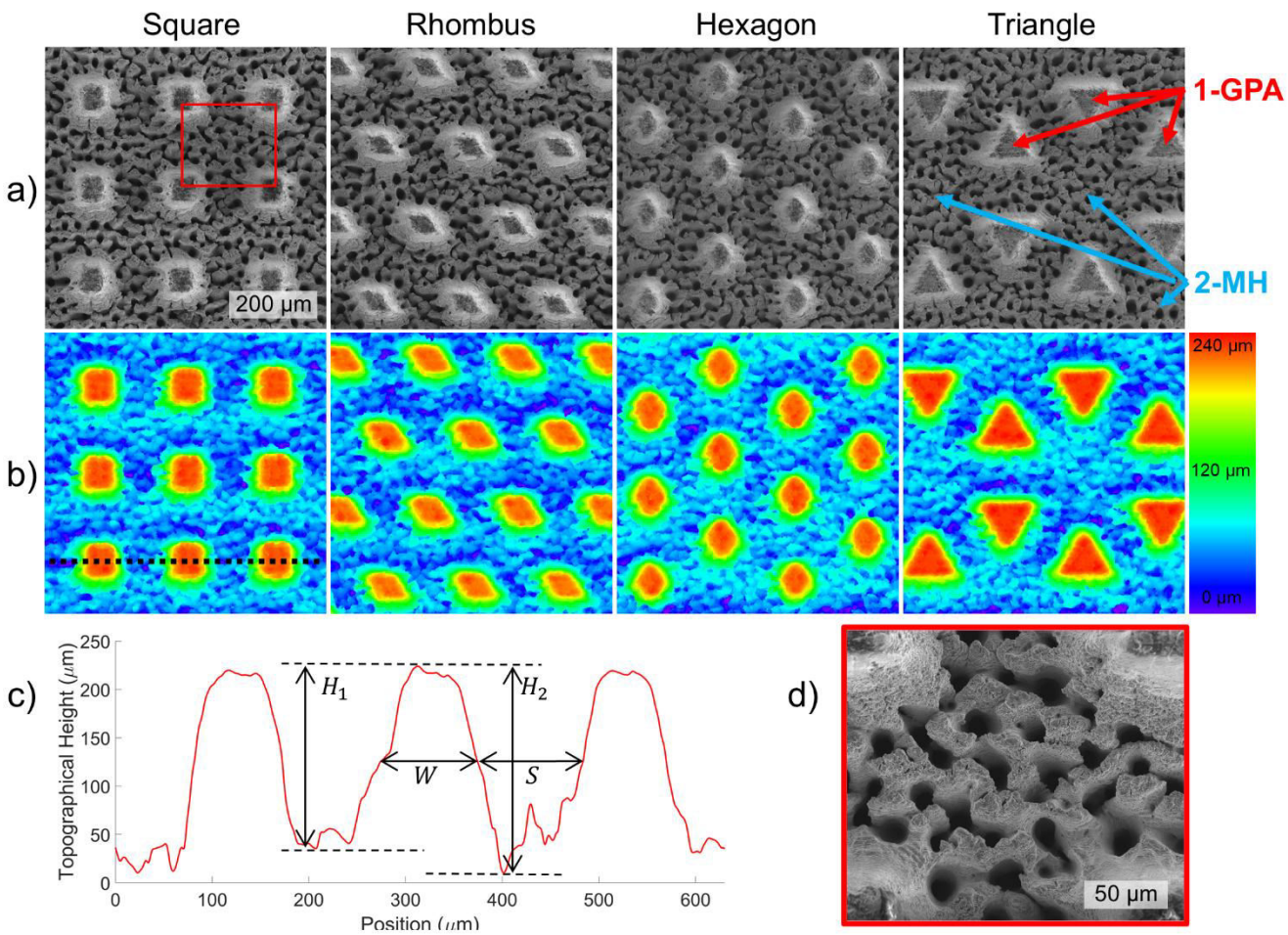

Figure 2. Microscopy images of the geometric topographies micromachined onto the mold insert. (a) SEM images. The scale bar in the first image corresponds to all images in parts a and b. The primary geometric pillar array (1-GPA) and secondary microhole (2-MH) substructure are identified by the coloured arrows. (b) Confocal microscope heatmap images. As indicated by the bar on the right, the colour within the images corresponds to the topographical height; blue indicates regions of low topographical height, whereas red indicates topographical peaks. (c) Topographical height data measured along the cross-section indicated by the dashed line in part b. The black lines indicate the measurement approach for the heights, widths, and spacings of the geometric microstructures. (d) Magnified SEM image of the area in the red box in part a, showing the microholes.

The width (W) and spacing (S) of the primary geometric pillar arrays were measured according to the full-width-half-maximum (FWHM) definition, as illustrated in **Figure 2(c)**. The heights of the pillars were measured from their highest peak to the lowest measured position of the adjacent valleys

on either side (H_1 and H_2). Then, H_1 and H_2 were averaged to obtain an average height value (H) for each geometry. **Table 1** lists the values of H and S for each geometric structure. The values are very consistent, with average values of $H = 193 \pm 8$ μm and $S = 100 \pm 4$ μm. **Table 1** also contains areal surface roughness (S_a) measurements of the microholes present in the valleys between the pillars of each pattern. Note that, as described in **Supporting Note 1**, this areal roughness measurement considers only the valley regions between the primary geometric pillars where the secondary microholes are present. The S_a values are fairly consistent among the different structures, with an average of $S_a = 6.0 \pm 0.7$ μm.

Table 1. Measured dimensions of inscribed geometric microstructures. The "shallow" and "deep" squares are discussed in section 3.5.

Geometry	Height (μm)	Spacing (μm)	S_a (μm)
Rhombus	189 ± 25	99 ± 9	6.1
Hexagon	191 ± 22	102 ± 10	5.6
Triangle	191 ± 24	98 ± 9	6.6
Square	198 ± 27	102 ± 10	5.9

2.3 Microinjection Molding

Micro-injection molding was performed using a commercially available Toshiba 90A injection molding machine (model ISG90V10-2B). This machine was chosen because it is representative of conventional (i.e. industrial) injection molding machines that can be fitted with microstructured molds to accomplish Category III μIM. Accordingly, as shown in **Figure 1(b)**, the mold insert was inserted into a slot in the larger steel mold, which forms a small ($12.3 \times 8.1 \times 6.3$ cm^3) pail as seen in **Figure 1(d)**. Note that each laser inscribed patch was positioned on the mold insert equidistant from the injection port, i.e. at 34 mm. This ensured that, during the injection phase, the polymer melt would arrive at each patch simultaneously and with equivalent pressure and temperature.

For all experiments, the injection time was 1.28 s, the packing time was 3.2 s, the cooling time was 9 s, and the cycle time was 20 s. The injection velocity was 50 mm/s, which corresponds to a screw speed of 298 RPM and a volume injection rate of 40 g/s. Since the molded pail has a wall thickness of 1.76 mm, these settings correspond to a melt advancement rate of 0.11 m/s at the location of the microstructured patches, with a shear rate of 378 s^{-1}. The molding parameters investigated were the holding pressure (P_{hold}), resin melt temperature (T_{melt}), and the mold temperature (T_{mold}). **Table 2** outlines the molding parameters that were tested in this report.

Table 2. Varied molding parameters

Setting #	P_{hold} (MPa)	T_{melt} (ºC)	T_{mold} (ºC)
1	0.92	213	27
2	1.83	213	27
3	3.67	213	27
4	5.50	213	27
5	1.83	204	27
6	1.83	229	27
7	1.83	213	16
8	1.83	213	38

Beyond the molding parameters, two different polypropylene resins were tested: polypropylene 66 (PP-66) and polypropylene 2071 (PP-2071). Their physical properties are outlined in **Table 3**. The values for their density and melt flow rate were obtained from the manufacturer's data sheets (LyondellBasell). The dynamic viscosity was measured on an ARES rheometer (TA Instrument inc.) using a parallel plate geometry (25 mm diameter). Strain sweeps were performed first to determine the limits of the linear viscoelastic (LVE) regime. Then, frequency sweeps (0.1-60 Hz) were performed at three temperatures (180, 200 and 220 °C) using a deformation of 5%. **Supporting Note 3** provides full

details of the small amplitude oscillation shear (SAOS) measurements (all data, including the calculated relaxation times for each resin and temperature tested). Note that the dynamic viscosities presented in **Table 3** were selected from this dataset as the temperature and frequency most relevant to the molding experiments.

Table 3. Physical properties of the polypropylene used.

Property:	PP-66	PP-2071
Density at 23 ºC (g/mL)	0.90 g/mL	0.90 g/mL
Dynamic Viscosity (220 ºC, 60 Hz)	137 Pa·s	67 Pa·s
Melt Flow Rate (230 ºC)	18 g/10 min	50 g/10 min

3 Results and Discussion

To organize our experimental results and the discussion surrounding them, we have separated our analysis into four main sections. First, SEM and confocal micrographs are presented in order to visualize the replicated polymer parts and establish an analysis protocol. Next, we examine the influence of different molding parameters including the holding pressure, mold temperature, and melt temperature on the replication fidelity of polypropylene 2071 replicates. The ensuing section (§3.3) presents the most novel part of this investigation, and analyzes the impact of varying the geometric pattern of the mold's primary pillar arrays. The final section tests a second polymer resin (polypropylene 66), to determine the influence of viscosity and melt flow index on the micro-injection molding process.

3.1 Characterization of Polymer Replicates

Figure 3(a) provides SEM micrographs of polymer replicates molded using polypropylene 2071 (PP-2071) at a holding pressure of $P_{hold} = 3.67$ MPa. Based on the nature of µIM, the topography of the replicate forms the inverse structure of the mold insert. Hence, where the mold consists of geometric

pillar arrays surrounded by secondary microholes, the polymer replicate consists of primary geometric cavity arrays (1-GCA) surrounded by peaks decorated with secondary "microbumps" (2-MB). These hierarchical structures are indicated by the coloured arrows in **Figure 3(a)**. The microbumps are the direct result of the injected polymer melt entering the mold's microholes, and match the patterns observed on the mold insert (**Figure 2(b)**). The structure of the polymer replicates are further visualized in **Figure 3(b)**, which presents confocal heatmaps of the same regions shown in **Figure 3(a)**.

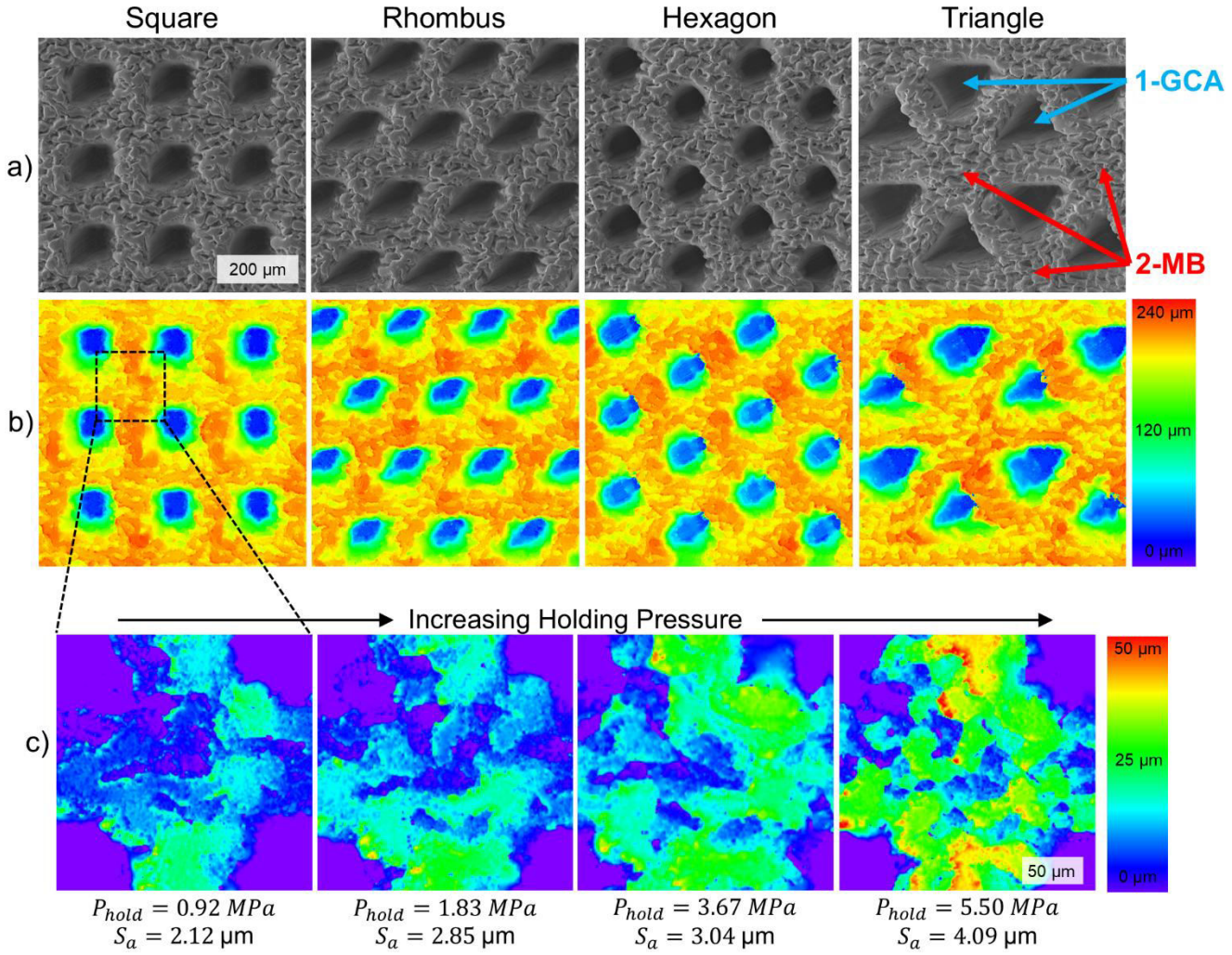

Figure 3. (a) SEM micrographs of polypropylene-2071 µIM polymer replicates ($\boldsymbol{P_{hold} = 3.67}$ **MPa**). The scale bar on the first image applies to all images in parts a and b. (b) Confocal microscope heatmaps of the same samples. (c) Confocal microscope heatmaps of the area indicated by the black box in part b, when molded at different holding pressures. The scale of the heatmap has been readjusted (compared to part b) to better visualize the differences.

3.2 Influence of Molding Parameters

As detailed in **Table 2**, we tested different holding pressures (P_{hold}), mold temperatures (T_{mold}), and polymer melt temperatures (T_{melt}) to asses their impact on the μIM process. To evaluate the influence of the holding pressure, each geometry was molded using PP-2071 at P_{hold} ranging from 0.92 to 5.50 MPa. We observed that the height of the secondary microbumps compared to the underlying material is positively correlated with P_{hold}. This relationship is visualized in **Figure 3(c)**, in which a magnified view of the square region indicated in **Figure 3(b)** is shown for four different holding pressures. In the left image ($P_{hold} = 0.92$ MPa), the microbumps are not very tall, as indicated by the widespread presence of blue in the confocal heatmap. However, as P_{hold} increases, each successive image shows progressively taller microbumps, as indicated by the appearance of more green, yellow, and eventually red in the heatmaps.

This observation can be quantified by considering the areal roughness (S_a) of the microbumps. Using data from molding settings 1 through 4 (**Table 2**), **Figure 3(c)** shows that S_a rises monotonically as P_{hold} increases, starting from $S_a = 2.12$ μm at $P_{hold} = 0.92$ MPa, and increasing to $S_a = 4.09$ μm at $P_{hold} = 5.50$ MPa. This positive trend occurs because high values of P_{hold} help to increase the penetration of the polymer into the mold's microholes, thereby increasing the height of the replicated microbumps [24, 41, 42]. Considering that this mechanism was detectable through roughness measurements, **Figure 3(c)** confirms that measuring S_a of the microbumps offers an indirect quantification of the overall replication fidelity of the smallest-scale structures, which are the most challenging to reproduce [43]. Accordingly, in the analysis below, the areal roughness will serve as our primary quantification method for the replication fidelity.

However, to accurately compare the influence of the molding parameters tested, we first note that the S_a values of the secondary microholes on the mold insert are similar for all four geometric

structures, but not exactly the same. As listed in **Table 1**, the values range from a minimum of $S_a = 5.6$ to a maximum of 6.6 μm for the different patches. To prevent these slight deviations from affecting our analysis, we will present the ensuing roughness data as the relative microbump height:

$$S_a^* = \frac{S_{a,replicate}}{S_{a,MI}} \qquad \text{Equation 2}$$

where $S_{a,replicate}$ is the areal average roughness of the microbumps on the polymer replicate surface, and $S_{a,MI}$ is the roughness value of the microholes on the corresponding mold insert patch. Accordingly, S_a^* quantifies the relative penetration of the polymer melt into the microholes of the mold, such that a value of $S_a^* = 0$ indicates no penetration, while $S_a^* = 1$ indicates that the molten polymer perfectly replicated the microholes into equally sized microbumps. Using this approach, the slight deviations in the microhole roughness of the different geometries inscribed on the mold can be effectively ignored in the following analysis.

Settings 1 through 4 in our experimental plan (**Table 2**) test a range of different P_{hold} values while maintaining constant values of T_{mold} and T_{melt}. **Figure 4(a)** shows the change in S_a^* for each of the four geometries tested for PP-2071. As was previously observed for square structures in **Figure 3(c)**, here we observe that S_a^* rises monotonically with P_{hold} for the other three geometries as well (rhombus, hexagon, triangle). Specifically, the average value of S_a^* among the different geometries tested rises dramatically from $S_a^* = 0.40$ to 0.70 over the range of holding pressures tested. This strong correlation is expected, since numerous reports have found that using a high holding pressure is an important factor in promoting good replication fidelity for microstructures [24, 41, 42].

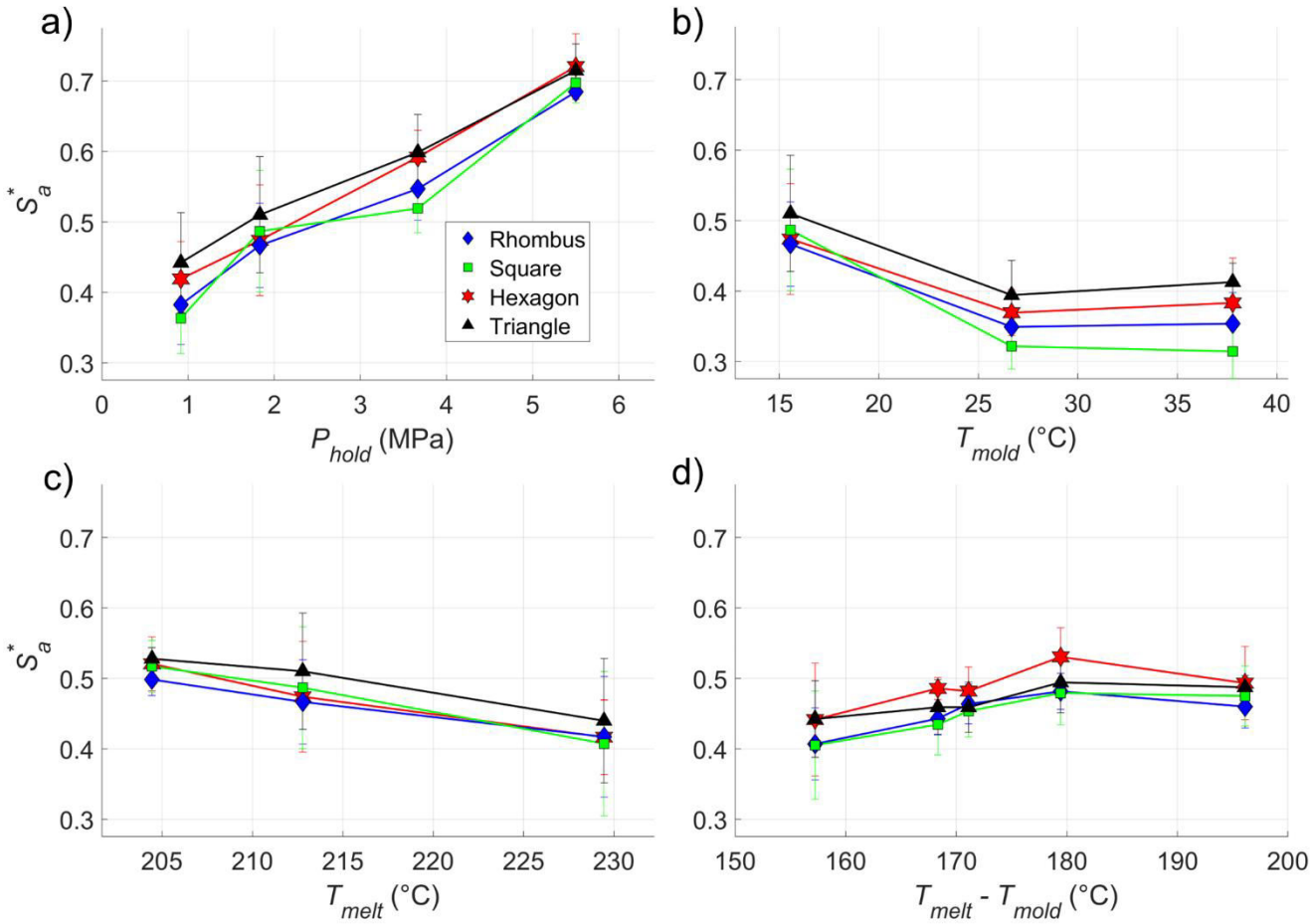

Figure 4. Influence of different molding parameters on the replication fidelity of PP-2071. (a) Influence of holding pressure. (b) Influence of melt temperature. (c) Influence of mold temperature. (d) Influence of the difference between $\boldsymbol{T_{melt}}$ and $\boldsymbol{T_{mold}}$.

Next, in **Figure 4(b-c)**, T_{mold} and T_{melt} are varied while the holding pressure is held constant at $P_{hold} = 1.83$ MPa. In **Figure 4(b)**, we see that S_a^* has a weak negative correlation with the mold temperature, dropping from an average value of $S_a^* = 0.48$ to 0.37 as T_{mold} increases from 16 to 38 ºC. A similar pattern emerges for the melt temperature in **Figure 4(c)**, in which S_a^* drops slightly from an average value of $S_a^* = 0.52$ to 0.42 as T_{melt} increases from 204 to 229 ºC. Finally, **Figure 4(d)** plots S_a^* as a function of $T_{melt} - T_{mold}$, which represents the driving force behind melt solidification with respect

to both temperature values. However, since no clear trend emerges from this plot, we conclude that $T_{melt} - T_{mold}$ is not correlated with the replication fidelity in our μIM process.

Interestingly, although the changes in S_a^* with T_{mold} and T_{melt} are both statistically significant (see **Supporting Table S3**), these findings contrast with previous studies. Numerous reports have found that higher T_{melt} leads to greater replication fidelity, since the molten polymer resin can be cooled further before beginning to solidify. This in turn reduces the impact of the hesitation effect, thereby promoting deeper penetration of the polymer into the smallest-scale mold cavities, which in our case would be the secondary microholes. A similar theory has been established for T_{mold}, where a higher mold temperature reduces the cooling rate of the molten polymer, which typically helps to improve replication fidelity by reducing the impact of the hesitation effect. However, these commonly observed positive correlations between the replication fidelity with respect to T_{mold} and T_{melt} are not present in our own data. Therefore, while it remains unclear exactly why a weak negative correlation is obtained, the trends observed in **Figure 4(b-c)** suggest that the hesitation effect is not a limiting factor in our μIM process.

This conclusion can be justified by estimating the solidification time (t_s) of the molten polymer in the mold cavity using Planck's equation:

$$t_s = \frac{\Delta H_c \rho}{(T_f - T_{mold})} \times \left(\frac{BL}{h} + \frac{BL^2}{4\kappa}\right) \qquad \text{Equation 3}$$

where ΔH_c is the latent heat of solidification, ρ is the polymer's density, T_f is the solidification temperature, L is the characteristic length, h is the heat transfer coefficient, κ is the thermal conductivity, and B is a coefficient which varies with the mold's geometry ($B = 0.5$ for parallel plates and $B = 0.25$ for a cylinder) [44]. For this estimate, we apply values of $\Delta H_c = 234$ kJ/kg [45], $\rho = 900$ kg/m^3 (**Table**

3), $T_f = 165$ ℃ [46], $\kappa = 0.26$ W/m·K [47], and the value of h can be estimated as κ/L (with units of W/m^2·K).

Note that Plank's equation is highly simplified, and assumes that there is a discrete solidification point, thermal conductivity has a constant value below t_s, and sensible heats are negligible. Nevertheless, **Equation 3** provides a rough estimate of the timescale of t_s at mold cavity locations with different length scales. Specifically, **Equation 3** predicts an approximate solidification time of $t_s \approx 11$ s in the macroscopic walls of the molded part ($L = 1.76$ mm), 37 ms within the spacing between pillars comprising the primary geometric pillar array ($L = S = 100$ μm), and 0.2 ms within the secondary microholes, for which we assume a cylindrical geometry ($L = 10$ μm). Given that $t_s \approx 11$ s within the macroscopic cavities, this analysis confirms that relatively little solidification occurs during the injection phase (1.28 s duration) of our molding process, which explains why the hesitation effect does not affect our results. However, the value of t_s is on the millisecond scale for the spaces between primary geometric pillars and within the secondary microholes. Hence, considering that we achieved good replication of these microscopic features, this analysis suggests that after the hesitation phase ended, the melt penetrated the microstructures very quickly.

The t_s values calculated above also give important information about the behaviour of the replicated part after molding. Notably, parts that still contain resin that is not completely solidified after molding may experience shrinkage or sink marks while they cool after ejection [48]. However, since the cooling time of our process (9 s) is much greater than t_s within the microstructures (millisecond scale), this analysis confirms that post-molding shrinkage does not affect our replicated microstructures. We note that it is possible that the macroscopic walls of the molded pail may not have fully frozen, since the estimated value of $t_s \approx 11$ s for those regions is only slightly smaller than the combined length of the injection, packing, and cooling phases (13.48 s, as per Section 2.3). However, even if that is the

case, shrinkage or void formation in that region would not affect the measured values of S_a^* on the microbumps. Hence, we conclude that polymer shrinkage does not affect our results.

3.3 Influence of Different Geometric Patterns

Looking back at **Figure 4(a-c)**, we observe that the geometric pattern of the pillar arrays has a noticeable influence on the replication fidelity. For example, in **Figure 4(a)**, the triangle pattern exhibits higher S_a^* values than the square, rhombus, and hexagon patterns in the range of $0.92 \leq P_{hold} \leq 3.67$ MPa. In contrast, the square and rhombus patterns exhibit comparatively poor replication fidelity. These geometries exhibit lower S_a^* values at each P_{hold} tested, with the exception of $P_{hold} = 1.83$ MPa, for which the square pattern performs uncharacteristically well. However, we note that this specific data point at $P_{hold} = 1.83$ MPa (setting #3 in **Table 2**) was the first experiment performed in the series of molding parameters tested, and therefore this outlier might be the result of a lack of steady state in the molding press.

To discern the statistical significance levels of the geometric pattern's influence, we performed a series of two-tailed student's t-tests, which determine the significance level (p-values) of differences between means. The results are listed in **Table 4**, which assesses each combination of geometries tested under high-P_{hold} and low-P_{hold} conditions. Note that **Table 4** applies asterisk notation to summarize the confidence intervals at a glance (* $p \leq 0.10$, ** $p \leq 0.05$, *** $p \leq 0.01$). According to the results, many of the separations between the data points of different geometries shown in **Figure 4(a)** are indeed statistically significant. Notably, at $P_{hold} = 0.92$ MPa, all 6 T-tests result in $p \leq 0.002$, which indicates at least 99.8% confidence. Considering that the different geometries tested had equivalent feature spacing and aspect ratios (**Table 1**), this analysis confirms that the microstructure's geometric pattern has a significant impact on the replication fidelity when molding at low holding pressures.

However, the geometric pattern plays less of a role at high holding pressures. At $P_{hold} = 5.50$ MPa, only 2 of the 6 *t*-tests (rhombus vs. hexagon and rhombus vs. triangle) determined statistically significant separations between the S_a^* values of the data points. This finding suggests that, while the geometric pattern does play a key role in the replication fidelity of μIM, its influence can be overshadowed by high holding pressures.

Table 4. p-values of *t*-test determining significance of separation between means. The data compares S_a^* for rhombus (Rh), hexagon (Hx), triangle (Tr), and square (Sq) geometries. The asterisk notation is defined in the main text.

Geometries	$P_{hold} =$ 0.92 MPa	$P_{hold} =$ 5 MPa
Rh vs. Sq	0.002 (***)	0.20
Rh vs. Hx	5×10^{-4} (***)	0.06 (*)
Rh vs. Tr	5×10^{-7} (***)	0.04 (**)
Sq vs. Hx	5×10^{-5} (***)	0.21
Sq vs. Tr	4×10^{-8} (***)	0.24
Hx vs. Tr	6×10^{-4} (***)	0.73

To determine why the geometric shape of the pillar array has a significant influence on the replication fidelity, we tested three different characteristics of their overall topography. First, we consider the solid fraction (SF), which we define as the fraction of each patch occupied by the peaks of the geometric pillars. As illustrated by the dashed blue lines in **Figure 5(a)**, this characteristic is relevant to the μIM process because it represents the area of solid/melt interface that allows for heat transfer during the injection phase (while the melt hesitates before penetrating the valleys between the primary pillars). **Figure 6(a)** plots S_a^* vs. SF and produces a relatively weak correlation ($R^2 = 0.64$), which indicates that S_a^* is not strongly correlated with SF.

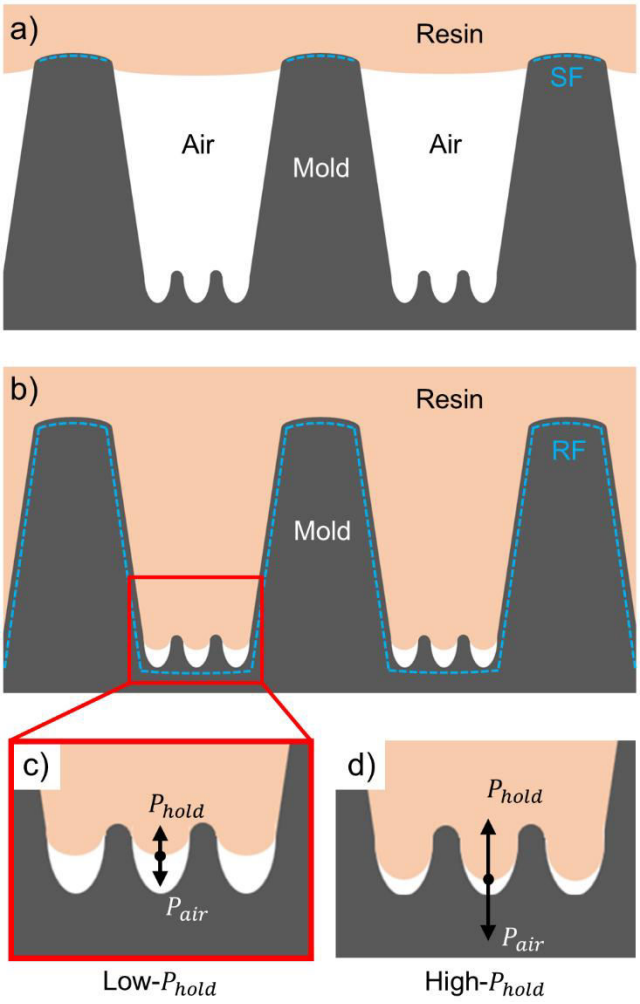

Figure 5. Schematic cross-section depicting the resin melt's interface with the mold. (a) During injection phase while the melt hesitates at the entrance of the primary geometric structure. (b) During the holding phase while the melt penetrates the secondary microholes. (c) Pressure balance at the air/melt interface within the microholes at low holding pressure. (d) Pressure balance at high holding pressure.

Next, we tested the influence of the roughness factor (RF) of each pattern, which we define as the ratio between the actual surface area of the peaks, valleys, and sidewalls of the geometric pillars versus the area of the mold surface when viewed from a "bird's eye" perspective. This dimensionless variable is equivalent to the roughness factor in Wenzel's seminal wetting model [49], and was measured using the Olympus Lext Analysis Application. The RF is visualized in **Figure 5(b)**, and is

relevant since it determines the surface area allowing for heat transfer during the holding phase, while the melt makes full contact with the walls of the cavities between the primary geometric pillars. **Figure 6(b)** plots the influence of the RF on S_a^*, which generates an R^2 value of only 0.08, indicating no correlation. Accordingly, both **Figure 6(a)** and **Figure 6(b)**, confirm our above hypothesis that heat transfer, and hence premature melt solidification (hesitation effect), is not a limiting factor in our μIM process.

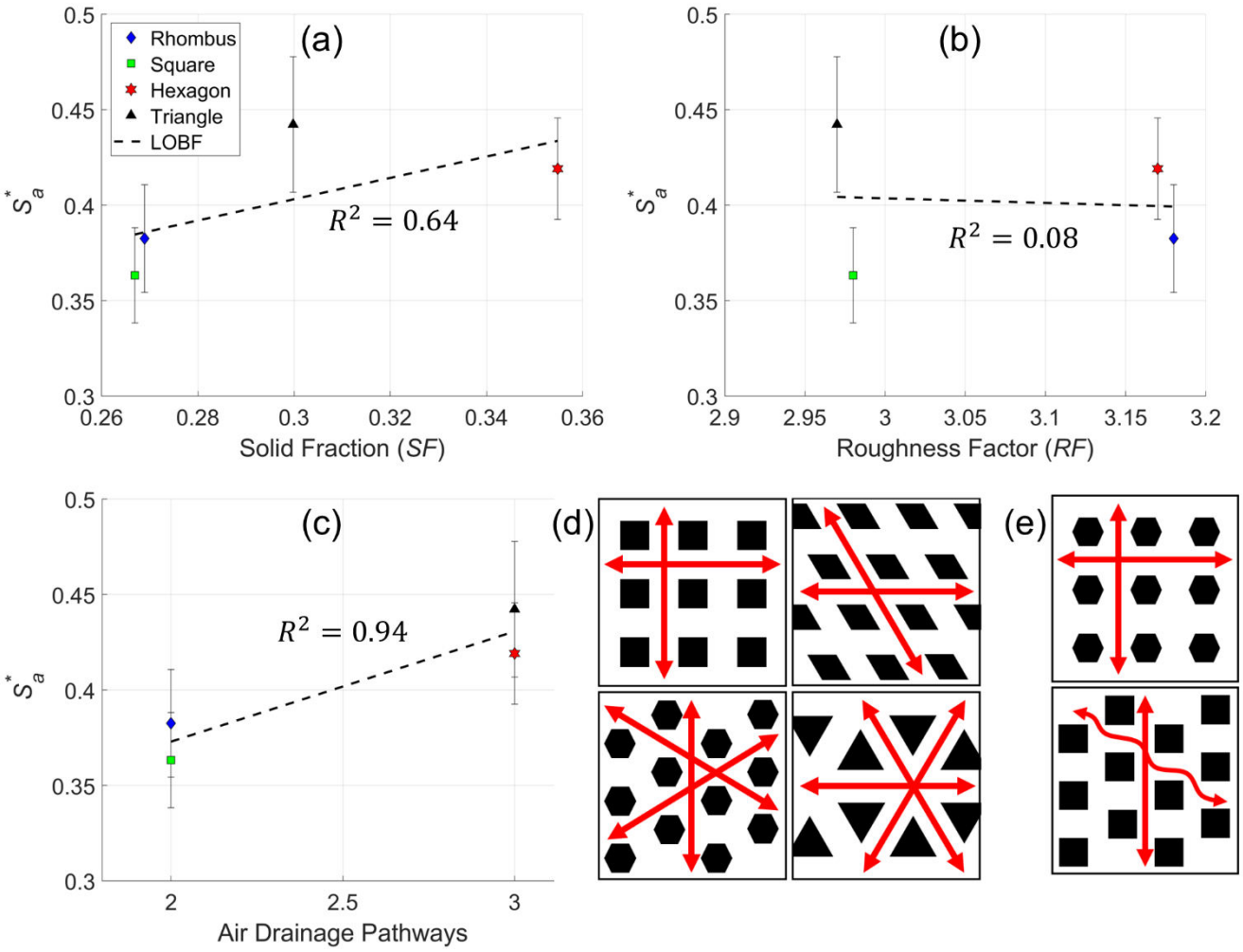

Figure 6. Correlation of the relative microbump height with different geometric factors. (a) Influence of the solid fraction. (b) Influence of the total surface area. (c) Influence of the number of major air drainage pathways of the array's geometry. (d) Schematic representation of major air drainage pathways. (e) Schematic representation of hexagonal features in a square array and square features in a hexagonal array.

In contrast, **Figure 6(c)** considers a very different characteristic of the geometric patterns tested: the number of linear pathways that air can use to drain out of the primary geometric pillar array during the injection phase. This concept is visualized in **Figure 6(d)**, which presents a schematic of the four different geometric pillar patterns inscribed on the mold's surface. Here, the black shapes represent the locations of micropillars and the white sections indicate the valleys between them (see **Figure 1**). As

shown by the red arrows, starting from any given intersection between pillars, the square and rhombus patterns allow for only two linear pathways through which air can escape the microstructure while the polymer melt fills the mold. In contrast, the triangle and hexagon patterns each have 3 linear pathways for air drainage. This difference is important because numerous reports on μIM have found that promoting effective air drainage is a crucial factor in obtaining high replication fidelity [2, 31, 32]. Accordingly, in our experiment, the effect of improved air drainage is apparent in **Figure 6(c)**, in which there is a strong correlation ($R^2 = 0.94$) between S_a^* and the number of drainage pathways. Specifically, the triangle and hexagon patterns (which each have 3 drainage paths) perform significantly better than the square and rhombic patterns (which have only 2 pathways). Therefore, we conclude that in the process of μIM, different geometric patterns of the microstructures can promote improved air drainage, which can in turn increase the replication fidelity of fabricated parts.

This conclusion is consistent with section 3.2 above, in which we found that S_a^* is not highly dependent on T_{melt} or T_{mold}, indicating that the hesitation effect is not a limiting factor in our μIM process. Instead, it seems that in our case the melt is not solidifying prematurely, but is prevented from reaching the deepest cavities of the secondary microholes by trapped air. This occurs because, as the melt is pressed into the valleys between the geometric pillars, any air that was unable to properly drain during the injection phase will be compressed until it reaches a pressure consistent with the holding pressure. This also explains why our measurements of S_a^* are greater at higher P_{hold}; with higher holding pressure, the trapped air is compressed to a higher pressure, and hence a lower volume. Thus, the air/melt interface is pushed further into the microholes, allowing the melt to form taller, higher roughness microbumps. This theory is visualized in **Figure 5(c)**, which presents a magnified view of **Figure 5(b)** at the air/melt interface within the microholes at different holding pressures. The black

arrows represent a pressure balance between P_{hold} and the air pressure (P_{air}) when the holding pressure is adjusted to different values.

As a last discussion point on the topic of air drainage, we note that the array patterns of our primary geometric pillar patterns match the shape of the pillars themselves. For example, the square pillars are arranged in a square array, and the hexagonal pillars are arranged in a hexagonal array. Based on the discussion above, we theorize that this approach is important to ensure effective air drainage during molding. For example, **Figure 6(e)** presents a schematic of the opposing case, where the array pattern does not match the microfeature shape. As shown by the red arrows, arranging hexagonal features in a square array would reduce the pattern's drainage pathways to only 2 (instead of 3 seen for hexagons in **Figure 6(d)**), thereby losing the air drainage benefits of hexagons altogether. Similarly, arranging square features in a hexagonal array would allow for only one unobstructed linear drainage pathway, while the diagonal paths that would normally be present for a hexagonal array are impeded by the corners of the square microstructures. This would likely lead to poor drainage and possibly even lower replication fidelity than we observed for the square array of square micropillars. Based on this argument, we predict that if a similar study was performed with such mismatching micropillar shape/array geometries, the replication fidelity would be reduced.

3.4 Influence of Polymer Resin

Our discussion so far has focused on our experimental results using PP-2071. In this section, we compare the influence of the same variables (molding parameters, geometric pattern) when using polypropylene 66 (PP-66), which has different physical properties. As listed in **Table 3**, PP-66's dynamic viscosity of $\eta = 137$ Pa·s is about twice as high as PP-2071's viscosity (67 Pa·s). This property is also reflected in PP-66's much lower melt flow rate of 18 g/10 min compared to PP-2071's value of

50 g/10 min. Both of these comparisons indicate that PP-2071 flows more easily than PP-66, which is why PP-2071 is often used in industrial settings to fabricate parts for which the mold is difficult to fill.

To further characterize the rheological properties of these two different polypropylene resins, we performed SAOS rheology tests to determine the relaxation time (t_{relax}) of the melts. The complete set of data is presented in **Supporting Note 3**. The range of t_{relax} was determined to be 17.5 to 30 ms for PP-2071 and t_{relax} = 27.3 to 65.1 ms for PP-66, across the temperature range tested. These values can be compared to the time required for the molten flow front to advance from one primary micropillar to the next. Given our injection rate of 40 g/s and the position of the patches (34 mm away from the injection gate), the advancement rate of the flow front was 0.11 m/s while the melt flowed over the inscribed patches. Considering an average pillar-to-pillar spacing of 200 μm (as per **Figure 2**), this corresponds to a time delay of only 1.8 ms for the advancing melt front to advance from one pillar peak to the next. Since this value is much lower than t_{relax}, this analysis indicates that the polymer chains did not have time to relax after interacting with each successive pillar in the geometric arrays. Accordingly, elastic effects can be ignored in this regime, since viscous forces are much more dominant.

Now, to assess how these differences in flow properties affect μIM, **Figure 7** compares the changes in S_a^* versus P_{hold}, T_{mold}, and T_{melt} for both polymers. Note that the data points represent average values across all four geometric patterns so as to not overcrowd the plots, but the complete set of data for each geometric pattern is available for PP-66 in **Supporting Note 4**. In **Figure 7(a-b)**, the overall trends seen for both resins are very similar, which indicates that P_{hold} and T_{mold} have a similar influence on both resins. Interestingly, at first glance **Figure 7(c)** appears to show a positive correlation between S_a^* and T_{melt} for PP-66, which contrasts with PP-2071. However, a statistical analysis reveals that the slight increase in R_a^* for PP-66 is not statistically significant (see **Supporting Table S4**). So it can be concluded that no clear trend between S_a^* and T_{melt} is evident for this resin.

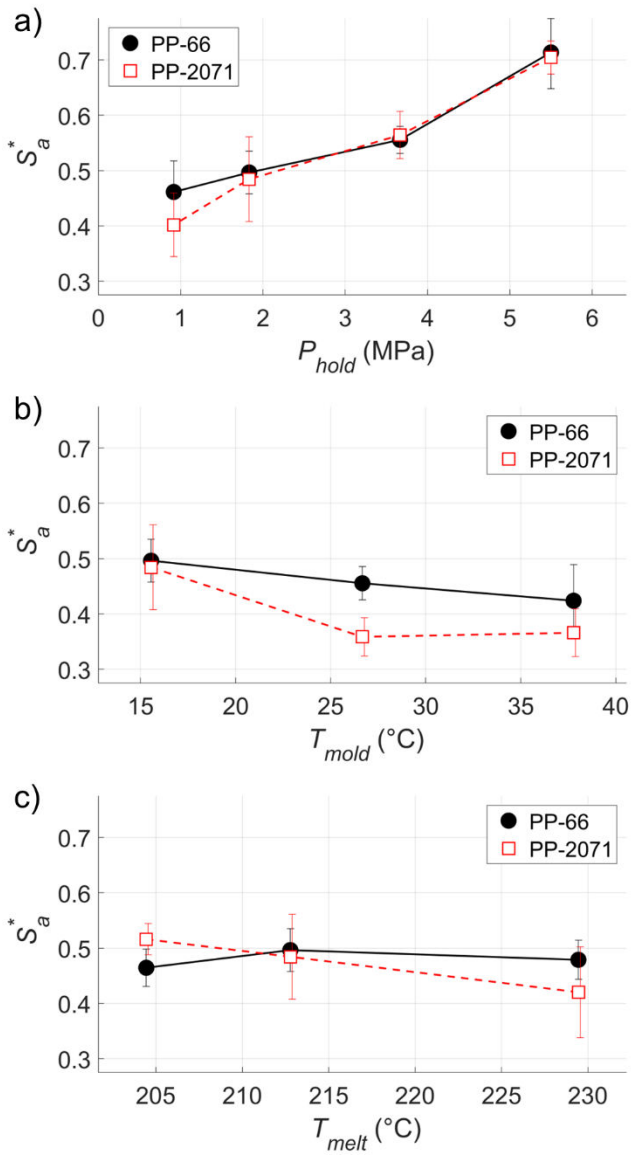

Figure 7. Comparison of polypropylene-66 and polypropylene-2071 polymer resins. (a) Influence of holding pressure. (b) Influence of mold temperature. (c) Influence of polymer resin melt temperature.

Considering that none of the plots in **Figure 7** demonstrate a statistically meaningful change in behaviour between PP-2071 and PP-66, we conclude that the viscosity and chain relaxation properties of the resin do not have a significant impact on our µIM process. Instead, as discussed above, our process is primarily governed by effective air drainage pathways and the holding pressure. This finding is

applicable to industrial processes since it shows that, while resins with a low melt flow rate are often selected as the material for hard to fill molds, this approach is ineffective when the macroscopic mold surfaces exhibit microtextures (category III μIM, as per the introduction).

4 Conclusions

Our results demonstrate that the geometric pattern of the mold's microstructure has a clear impact on the replication fidelity of the finished part. Specifically, patterns such as triangles and hexagons, which provide more channels for air drainage, offer improved performance over squares and rhombuses. This effect is most significant at low holding pressures, at which the trapped air pockets occupy a large volume within the smallest, most difficult to fill cavities of the mold. In contrast, high holding pressures can be applied to overcome this problem by compressing any trapped air into a smaller volume.

Still, the most effective solution to relieve air drainage problems in μIM is to install an evacuation system to remove all gases from the mold cavity (appropriate venting). However, these systems increase the cost of production and add complexity to the system, which has led to limited adoption in industry [42]. Therefore, our findings are most applicable towards improving mold design for Category III μIM processes, where a larger part is decorated with functional microstructures. As such, our results are mainly applicable for guiding mold design choices for industrial scale manufacturing of functionalized products. For such cases, where evacuation is not absolutely required, our findings demonstrate that the μIM performance can be improved by choosing a microstructure pattern with good drainage properties.

For future work, the influence of different geometric patterns should be tested using a broader range of polymer resins, including at least one amorphous polymer, to learn more about the generality

of our findings. In addition, it would be valuable to perform a similar set of experiments using a mold combined with the Variotherm technology, to determine whether rapid heat cycling can remove the limitations of geometric micropattern arrays with poor air drainage.

CRediT Author Statement

Damon G. K. Aboud: Conceptualization, Software, Formal Analysis, Investigation, Writing – Original Draft, Visualization. **Nicole Demarquette**: Conceptualization, Writing - Review & Editing. **Denis Rodrigue**: Formal Analysis, Investigation, Writing - Original Draft, Writing - Review & Editing. **Anne-Marie Kietzig**: Conceptualization, Writing - Review & Editing, Project administration, Supervision, Funding Acquisition.

Acknowledgements

The authors would like to thank Prof. Andrew Hrymak for his insightful comments and discussion about our experimental results. We also thank Francis Côté, Charles Grégoire, and Stéphane Mercier for their helpful contributions to this project.

Conflict of Interest Statement

The authors declare that no competing interests exist.

Data Access

Supplementary material is available online. The document includes: explanation of roughness measurement protocol, statistical analysis, small amplitude oscillation shear (SAOS) measurements, and plots for polypropylene 66.

Funding

This work was supported by the Natural Sciences and Engineering Research Council of Canada [NSERC CRD 543630–19]; the M-ERA.NET [M.ERA.NET 7205]; and the Pôle de recherche et d'innovation en matériaux avancés du Québec [PRIMA Québec].

References

[1] Whiteside B, Martyn M, Coates PD, Allan P, Hornsby P, Greenway G. *Micromoulding: process characteristics and product properties.* Plast. Rubber and Compos., 2003. **32**: 231-239.

[2] Gornik C. *Injection moulding of parts with microstructured surfaces for medical applications*. in *Macromol. Symp.* 2004. Wiley Online Library.

[3] Saarikoski I, Joki-Korpela F, Suvanto M, Pakkanen TT, Pakkanen TA. *Superhydrophobic elastomer surfaces with nanostructured micronails.* Surf. Sci., 2012. **606**: 91-98.

[4] Huovinen E, Takkunen L, Korpela T, Suvanto M, Pakkanen TT, Pakkanen TA. *Mechanically robust superhydrophobic polymer surfaces based on protective micropillars.* Langmuir, 2014. **30**: 1435-1443.

[5] Puukilainen E, Rasilainen T, Suvanto M, Pakkanen TA. *Superhydrophobic polyolefin surfaces: controlled micro-and nanostructures.* Langmuir, 2007. **23**: 7263-7268.

[6] Huovinen E, Hirvi J, Suvanto M, Pakkanen T. *Micro–micro hierarchy replacing micro–nano hierarchy: a precisely controlled way to produce wear-resistant superhydrophobic polymer surfaces.* Langmuir, 2012. **28**: 14747-14755.

[7] Wimberger-Friedl R. *Injection molding of sub-(mu) m grating optical elements.* J. of Inject. Molding Tech., 2000. **4**: 78.

[8] Gale M. *Replication techniques for diffractive optical elements.* Microelecton. Eng., 1997. **34**: 321-339.

[9] Kalima V, Pietarinen J, Siitonen S, Immonen J, Suvanto M, Kuittinen M, Mönkkönen K, Pakkanen TT. *Transparent thermoplastics: Replication of diffractive optical elements using micro-injection molding.* Opt. Mater., 2007. **30**: 285-291.

[10] Kuhn S, Burr A, Kübler M, Deckert M, Bleesen C. *Study on the replication quality of micro-structures in the injection molding process with dynamical tool tempering systems.* Microsyst. Tech., 2010. **16**: 1787-1801.

[11] Christiansen AB, Clausen JS, Mortensen NA, Kristensen A. *Injection moulding antireflective nanostructures.* Microelecton. Eng., 2014. **121**: 47-50.

[12] Yanagishita T, Masui M, Ikegawa N, Masuda H. *Fabrication of polymer antireflection structures by injection molding using ordered anodic porous alumina mold.* J. of Vac. Sci. & Tech. B, 2014. **32**: 021809.

[13] Becker H, Gärtner C. *Polymer microfabrication technologies for microfluidic systems.* Anal. and Bioanalytical Chem., 2008. **390**: 89-111.
[14] Attia UM, Marson S, Alcock JR. *Micro-injection moulding of polymer microfluidic devices.* Microfluid. and Nanofluidics, 2009. **7**: 1-28.
[15] Ma X, Li R, Jin Z, Fan Y, Zhou X, Zhang Y. *Injection molding and characterization of PMMA-based microfluidic devices.* Microsyst. Tech., 2020. **26**: 1317-1324.
[16] Gadegaard N, Mosler S, Larsen NB. *Biomimetic polymer nanostructures by injection molding.* Macromol. Mater. and Eng., 2003. **288**: 76-83.
[17] McMurray RJ, Gadegaard N, Tsimbouri PM, Burgess KV, McNamara LE, Tare R, Murawski K, Kingham E, Oreffo ROC, Dalby M. *Nanoscale surfaces for the long-term maintenance of mesenchymal stem cell phenotype and multipotency.* Nat. Mater., 2011. **10**: 637-644.
[18] Tsimbouri P, Gadegaard N, Burgess K, White K, Reynolds P, Herzyk P, Oreffo R, Dalby MJ. *Nanotopographical effects on mesenchymal stem cell morphology and phenotype.* J. of Cell. Biochem., 2014. **115**: 380-390.
[19] Cha KJ, Na M-H, Kim HW, Kim DS. *Nano Petri dishes: a new polystyrene platform for studying cell-nanoengineered surface interactions.* J. of Micromechanics and Microengineering, 2014. **24**: 055002.
[20] Gnilitskyi I, Alnusirat W, Sorgato M, Orazi L, Lucchetta G. *Effects of anisotropic and isotropic LIPSS on polymer filling flow and wettability of micro injection molded parts.* Opt. and Laser Tech., 2023. **158**: 108795.
[21] Komuro R, Kobayashi K, Taniguchi T, Sugimoto M, Koyama K. *Wall slip and melt-fracture of polystyrene melts in capillary flow.* Polym., 2010. **51**: 2221-2228.
[22] Awati KM, Park Y, Weisser E, Mackay ME. *Wall slip and shear stresses of polymer melts at high shear rates without pressure and viscous heating effects.* J. of Non-Newtonian Fluid Mech., 2000. **89**: 117-131.
[23] Griffiths C, Dimov S, Rees A, Dellea O, Gavillet J, Lacan F, Hirshy H. *A novel texturing of micro injection moulding tools by applying an amorphous hydrogenated carbon coating.* Surf. and Coat. Tech., 2013. **235**: 1-9.
[24] Masato D, Sorgato M, Lucchetta G. *Analysis of the influence of part thickness on the replication of micro-structured surfaces by injection molding.* Mater. and Des., 2016. **95**: 219-224.
[25] Xu G, Yu L, Lee LJ, Koelling KW. *Experimental and numerical studies of injection molding with microfeatures.* Polym. Eng. and Sci., 2005. **45**: 866-875.
[26] Baruffi F, Gülçür M, Calaon M, Romano J-M, Penchev P, Dimov S, Whiteside B, Tosello G. *Correlating nano-scale surface replication accuracy and cavity temperature in micro-injection moulding using in-line process control and high-speed thermal imaging.* J. of Manuf. Process., 2019. **47**: 367-381.
[27] Hobæk TC, Matschuk M, Kafka J, Pranov HJ, Larsen NB. *Hydrogen silsesquioxane mold coatings for improved replication of nanopatterns by injection molding.* J. of Micromechanics and Microengineering, 2015. **25**: 035018.
[28] Zhou M, Xiong X, Jiang B, Weng C. *Fabrication of high aspect ratio nanopillars and micro/nano combined structures with hydrophobic surface characteristics by injection molding.* Appl. Surf. Sci., 2018. **427**: 854-860.
[29] Sha B, Dimov S, Griffiths C, Packianather MS. *Micro-injection moulding: Factors affecting the achievable aspect ratios.* The Int. J. of Adv. Manuf. Tech., 2007. **33**: 147-156.

[30] Giboz J, Copponnex T, Mélé P. *Microinjection molding of thermoplastic polymers: a review.* J. of Micromechanics and Microengineering, 2007. **17**: R96.
[31] Su Y-C, Shah J, Lin L. *Implementation and analysis of polymeric microstructure replication by micro injection molding.* J. of Micromechanics and Microengineering, 2003. **14**: 415.
[32] Griffiths C, Dimov SS, Scholz S, Tosello G. *Cavity air flow behavior during filling in microinjection molding.* J. Manuf. Sci. Eng., 2011. **133**: 011006.
[33] Liparoti S, Sorrentino A, Titomanlio G. *Temperature and pressure evolution in fast heat cycle injection molding.* Materials and Manufacturing Processes, 2019. **34**: 422-430.
[34] Zhou S, Du M, Jariyavidyanont K, Zhuravlev E, Zou H, Androsch R, Schick C, Hrymak AN, Zhang R. *Interplay between chain relaxation time and melt crystallization time in microinjection molding of polyoxymethylene.* Macromolecules, 2024. **57**: 5780-5787.
[35] Wang Y, Weng C, Deng Z, Sun H, Jiang B. *Fabrication and performance of nickel-based composite mold inserts for micro-injection molding.* Appl. Surf. Sci., 2023. **615**: 156417.
[36] Romano J-M, Gulcur M, Garcia-Giron A, Martinez-Solanas E, Whiteside BR, Dimov SS. *Mechanical durability of hydrophobic surfaces fabricated by injection moulding of laser-induced textures.* Appl. Surf. Sci., 2019. **476**: 850-860.
[37] Ahmmed KT, Ling EJY, Servio P, Kietzig A-M. *Introducing a new optimization tool for femtosecond laser-induced surface texturing on titanium, stainless steel, aluminum and copper.* Opt. and Lasers in Eng., 2015. **66**: 258-268.
[38] Lv T, Cheng Z, Zhang D, Zhang E, Zhao Q, Liu Y, Jiang L. *Superhydrophobic surface with shape memory micro/nanostructure and its application in rewritable chip for droplet storage.* ACS Nano, 2016. **10**: 9379-9386.
[39] Tang Y, Yang X, Li Y, Lu Y, Zhu D. *Robust micro-nanostructured superhydrophobic surfaces for long-term dropwise condensation.* Nano Lett., 2021. **21**: 9824-9833.
[40] Kim DH, Seo CH, Han K, Kwon KW, Levchenko A, Suh KY. *Guided cell migration on microtextured substrates with variable local density and anisotropy.* Adv. Funct. Mater., 2009. **19**: 1579-1586.
[41] Pirskanen J, Immonen J, Kalima V, Pietarinen J, Siitonen S, Kuittinen M, Mönkkönen K, Pakkanen T, Suvanto M, Pääkkönen E. *Replication of sub-micrometre features using microsystems technology.* Plast. Rubber and Compos., 2005. **34**: 222-226.
[42] Lucchetta G, Sorgato M, Carmignato S, Savio E. *Investigating the technological limits of micro-injection molding in replicating high aspect ratio micro-structured surfaces.* CIRP Ann., 2014. **63**: 521-524.
[43] Wu P, Cheng C-W, Chang C, Wu T, Wang J. *Fabrication of large-area hydrophobic surfaces with femtosecond-laser-structured molds.* J. of Micromechanics and Microengineering, 2011. **21**: 115032.
[44] Pham Q. *Extension to Planck's equation for predicting freezing times of foodstuffs of simple shapes.* International Journal of Refrigeration, 1984. **7**: 377-383.
[45] Zarkadas D, Xanthos M. *Prediction of cooling time in injection molding by means of a simplified semianalytical equation.* Advances in Polymer Technology: Journal of the Polymer Processing Institute, 2003. **22**: 188-208.
[46] Turley S, Keskkula H. *Study of polypropylene annealed at a temperature near its melting point.* Journal of Applied Polymer Science, 1965. **9**: 2693-2706.
[47] Weidenfeller B, Höfer M, Schilling FR. *Thermal conductivity, thermal diffusivity, and specific heat capacity of particle filled polypropylene.* Composites Part A: applied science and manufacturing, 2004. **35**: 423-429.

[48] Singh Solanki B, Sheorey T, Singh H. *Experimental and numerical investigation of shrinkage and sink marks on injection molded polymer gears: A case study.* International Journal on Interactive Design and Manufacturing (IJIDeM), 2022. **16**: 1653-1667.
[49] Wenzel RN. *Resistance of solid surfaces to wetting by water.* Ind. & Eng. Chem., 1936. **28**: 988-994.

Enhanced micro-injection molding performance of geometric microstructure arrays

Damon G.K. Aboud[1], Nicole Demarquette[2], Denis Rodrigue[3], Anne-Marie Kietzig[1]*

[1] Department of Chemical Engineering, McGill University, Montreal, Quebec, Canada
[2] Department of Mechanical Engineering, Ecole de Technologie Supérieure, Montréal, Québec, Canada
[3] Department of Chemical Engineering, Laval University, Québec, Canada

*Corresponding author: anne.kietzig@mcgill.ca

Supporting Note 1: Explanation of Roughness Measurement Protocol

To measure the roughness of the injection molded microbumps, the first step is to identify regions of interest (ROIs) that contain only microbumps, and not the larger-scale holes. **Figure S1** shows screenshots from our custom-built MATLAB code, which automatically identifies the ROIs and measures the areal roughness in only that area. In **Figure S1**, the holes are visible as the large blue shapes in the first row of images, while the microbumps are represented by the red/orange area between them. In the second row, MATLAB's "*bwareaopen"* function is used to identify connected areas of pixels with low height values, which correspond to the holes to be avoided. Then, in the third row, the x/y positions of the holes are used to identify 40-pixel wide bands of height data for which the roughness will be measured. Note that the colormap has been rescaled in this row to better visualize the height data.

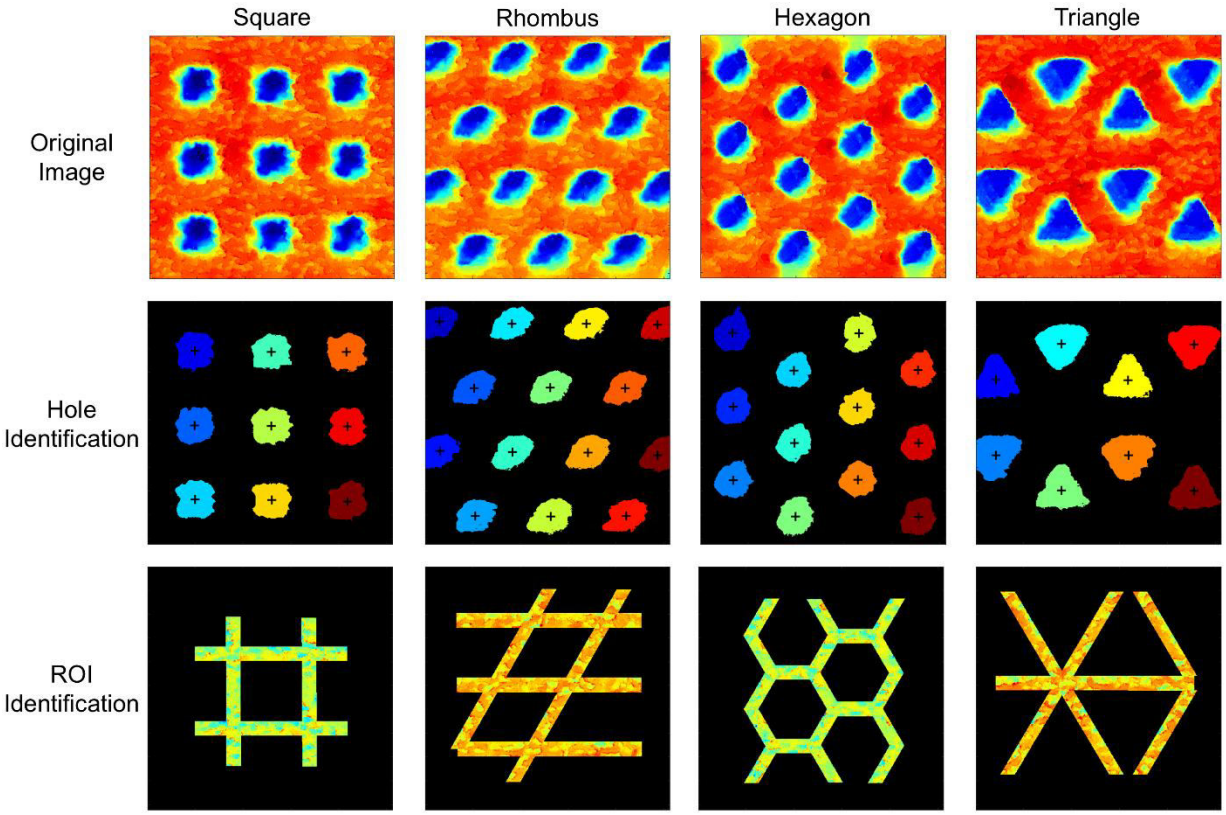

Figure S1. Visualization of steps in ROI identification.

Next, with the ROIs identified, the areal roughness can be measured. **Figure S2** shows a screenshot of the graphical user interface (GUI) from which the images in **Figure S1** were extracted.

The code first performs a form removal step to remove larger-scale trends in the height data (as is visible in **Figure S2(b)**). This step ensures that large "hills" in the topography of the molded replicate do not overshadow the actual roughness data, and is accomplished by applying a smoothing splines line fit to the data using MATLAB's "*fit*" function, with a form removal factor of 5×10^{-6} (as indicated by **Figure S2(a)**). The resulting roughness profile and R_a measurement is shown in **Figure S2(c)**.

After form removal, the code measures the areal roughness (R_a) of the ROI according to the arithmetical mean height definition,

$$S_a = \frac{1}{A} \iint_A |z(x, y)| \, dx \, dy$$

in which A is the measurement area, and $z(x, y)$ is the height (z) deviation at position (x, y) from the mean z-value of the surrounding topography. Note that, since the structures being compared through this method are all comprised of "microbump" structures of similar shape (but with varying bump height), using one definition for roughness (S_a) is sufficient in this case, whereas additional roughness definitions (such as the root mean square or maximum peak definitions) would be necessary to characterize topographical structures with entirely different shapes.

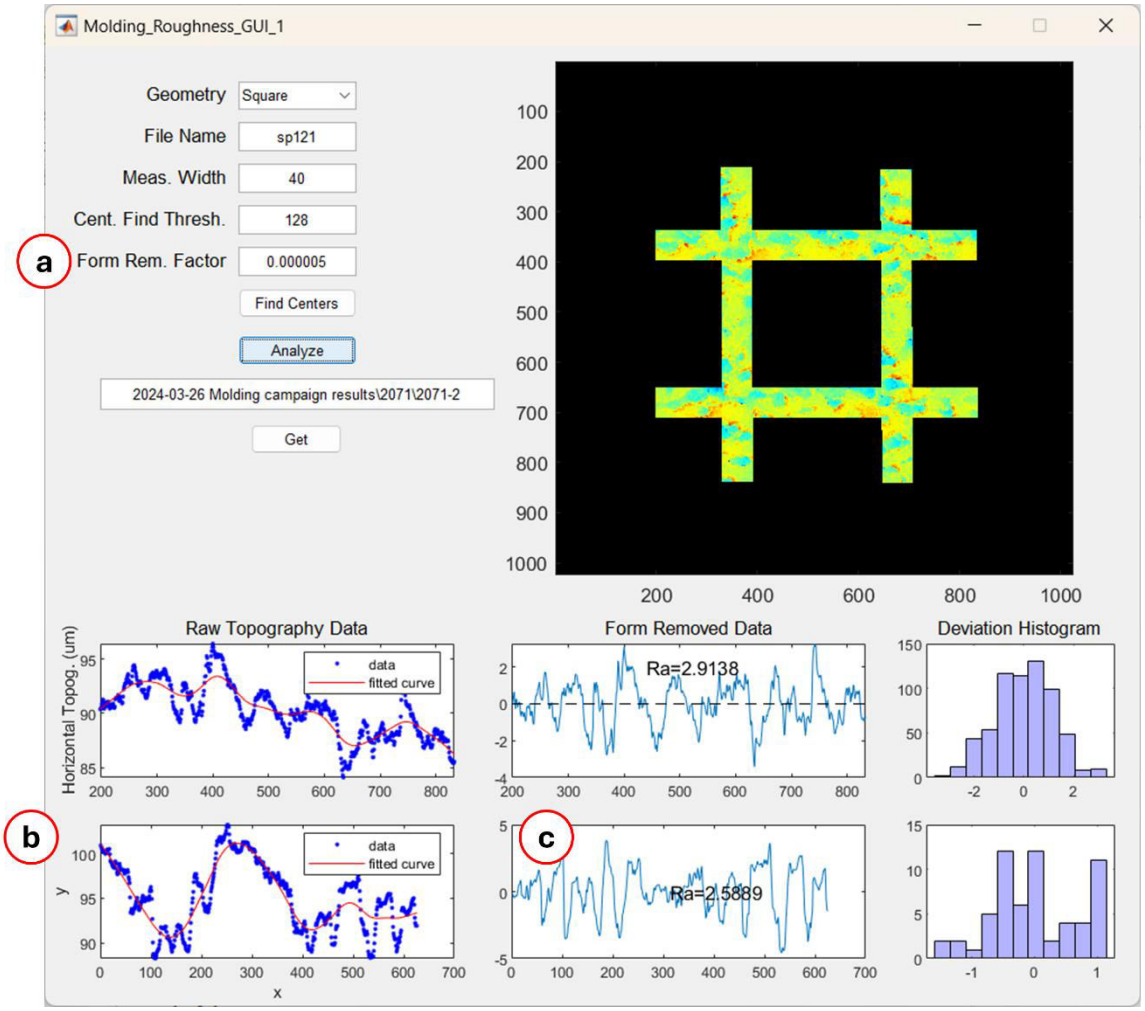

Figure S2. Full screenshot of the roughness measurement GUI. (a) Value of form removal factor. (b) Raw topography data. (c) Form-removed topography data.

Supporting Note 2: Statistical Analysis

The following tables offer two-tailed student's *t*-tests, which determine the confidence of the separation between means. Low *p-values* indicate high confidence. Green values indicate $p < 0.05$ (95% confidence), yellow indicates $0.05 < p < 0.10$, and red indicates $p > 0.10$. In **Tables S1** and **S2**, the letters R, T, S, and H indicate the rhombus, triangle, square, and hexagon patterns, respectively.

Table S1. Comparing different geometric structures for PP-2071 resin

$P_{hold} = 0.92$ MPa

Pattern:	R	T	R	S	R	H	S	H	S	T	H	T
R_a^*	0.38	0.45	0.38	0.37	0.38	0.42	0.37	0.42	0.37	0.45	0.42	0.45
	0.38	0.45	0.38	0.36	0.38	0.42	0.36	0.42	0.36	0.45	0.42	0.45
		0.46		0.36		0.41	0.36	0.41	0.36	0.46	0.41	0.46
	0.38	0.45	0.38	0.36	0.38		0.36		0.36	0.45		0.45
	0.38	0.44	0.38	0.36	0.38		0.36		0.36	0.44		0.44
p-value	5.E-07		0.00161		5.E-04		5.E-05		4.E-08		6.E-04	

$P_{hold} = 5.50$ MPa

Pattern:	R	T	R	S	R	H	S	H	S	T	H	T
R_a^*	0.69	0.70	0.69	0.68	0.69	0.71	0.68	0.71	0.68	0.70	0.71	0.70
	0.68	0.73	0.68	0.71	0.68	0.75	0.71	0.75	0.71	0.73	0.75	0.73
	0.69	0.73	0.69	0.70	0.69	0.70	0.70	0.70	0.70	0.73	0.70	0.73
		0.70								0.70		0.70
p-value	0.04388		0.20510		0.05682		0.21489		0.23960		0.73733	

Table S2. Comparing different geometric structures for PP-66 resin

$P_{hold} = 0.92$ MPa

Pattern:	R	T	R	S	R	H	S	H	S	T	H	T
R_a^*	0.47	0.51	0.47	0.48	0.47	0.53	0.48	0.53	0.48	0.51	0.53	0.51
	0.42	0.43	0.42	0.40	0.42	0.53	0.40	0.53	0.40	0.43	0.53	0.43
	0.41	0.51	0.41	0.50	0.41	0.53	0.50	0.53	0.50	0.51	0.53	0.51
	0.47	0.42	0.47	0.40	0.47		0.40		0.40	0.42		0.42
		0.50		0.49			0.49		0.49	0.50		0.50
p-value	0.25695		0.69473		0.00895		0.03329		0.46678		0.07877	

$P_{hold} = 5.50$ MPa

Pattern:	R	T	R	S	R	H	S	H	S	T	H	T
R_a^*	0.64	0.68	0.64	0.69	0.64	0.72	0.69	0.72	0.69	0.68	0.72	0.68
	0.70	0.73	0.70	0.74	0.70	0.77	0.74	0.77	0.74	0.73	0.77	0.73
	0.65	0.67	0.65	0.71	0.65	0.69	0.71	0.69	0.71	0.67	0.69	0.67
	0.69	0.72	0.69	0.78	0.69	0.73	0.78	0.73	0.78	0.72	0.73	0.72
	0.72	0.73	0.72	0.78	0.72	0.74	0.78	0.74	0.78	0.73	0.74	0.73
p-value	0.20021		0.02185		0.03227		0.65172		0.13142		0.22514	

Table S3. Comparing different mold and resin temperatures for PP-2071 resin

	Hexagon		Rhombus		Square		Triangle	
T_{mold} (ºC)	16	38	16	38	16	38	16	38
R_a^*	0.44	0.35	0.42	0.32	0.44	0.30	0.46	0.39
	0.47	0.37	0.47	0.37	0.50	0.31	0.53	0.42
	0.46	0.36	0.48	0.34	0.52	0.31	0.54	0.41
	0.53	0.41	0.49	0.37		0.34		0.43
		0.43		0.37				0.41
p-value	0.00636		0.00032		0.00078		0.00227	
	Hexagon		Rhombus		Square		Triangle	
T_{melt} (ºC)	204	229	204	229	204	229	204	229
R_a^*	0.51	0.42	0.49	0.27	0.50	0.39	0.52	0.42
	0.53	0.44	0.50	0.43	0.52	0.46	0.53	0.51
	0.49	0.39	0.49	0.45	0.50	0.44	0.52	0.42
	0.54		0.51	0.37	0.54	0.35	0.54	0.41
	0.53		0.51		0.52		0.53	
p-value	0.00062		0.01332		0.00279		0.00296	

Table S4. Comparing different mold and resin temperatures for PP-66 resin

	Hexagon		Rhombus		Square		Triangle	
T_{mold} (ºC)	16	38	16	38	16	38	16	38
R_a^*	0.51	0.42	0.48	0.40	0.48	0.39	0.47	0.42
	0.51	0.48	0.46	0.44	0.45	0.44	0.47	0.47
	0.54	0.41	0.48	0.39	0.49	0.36	0.51	0.43
	0.56	0.49	0.49	0.43	0.50	0.43	0.52	0.48
	0.53	0.41	0.49	0.38			0.50	0.42
p-value	0.00222		0.00038		0.01602		0.00986	
	Hexagon		Rhombus		Square		Triangle	
T_{melt} (ºC)	204	229	204	229	204	229	204	229
R_a^*	0.45	0.47	0.44	0.45	0.47	0.44	0.48	0.45
	0.49	0.47	0.46	0.46	0.46	0.45	0.48	0.45
	0.50	0.50	0.48	0.45	0.46	0.49	0.48	0.48
	0.49	0.53	0.47	0.49	0.51	0.45	0.50	0.45
	0.48	0.48	0.47	0.45	0.47	0.44	0.49	0.48
p-value	0.43801		0.69972		0.12552		0.01171	

Supporting Note 3: Small Amplitude Oscillation Shear (SAOS) Measurements

In this characterization technique, the value of $Tan\ Delta$ is the ratio of the loss modulus (G'', in Pa) to the storage modulus (G', also in Pa) of the polymer resin, such that $Tan\ Delta = G''/G'$. The relaxation time (t_{relax}) is the inverse of the frequency at which $Tan\ Delta = 1$ (i.e. $G'' = G'$). In the tables below, the highlighted cells represent the data points that were used to interpolate the value of t_{relax}.

Table S4. SOAS data for PP-2071

	$T = 180$℃		$T = 200$℃		$T = 220$℃	
Frequency (Hz)	Tan Delta	η (Pa·s)	Tan Delta	η (Pa·s)	Tan Delta	η (Pa·s)
60.0	0.71	122.0	0.83	94.9	0.96	67.4
37.9	0.94	164.3	1.10	124.3	1.28	86.7
23.9	1.12	205.9	1.32	151.7	1.53	103.5
15.1	1.28	251.6	1.53	179.9	1.79	120.8
9.51	1.45	302.0	1.76	209.7	2.08	139.0
6.00	1.65	356.4	2.04	240.9	2.42	156.5
3.79	1.88	413.2	2.38	270.2	2.84	173.4
2.39	2.17	471.2	2.80	297.8	3.37	189.2
1.51	2.51	528.7	3.33	323.2	4.04	203.5
0.95	2.93	584.3	3.98	345.5	4.89	216.4
0.60	3.49	634.1	4.84	364.9	5.98	227.0
0.38	4.16	681.4	5.94	381.0	7.43	236.2
0.24	5.01	722.0	7.39	394.8	9.08	243.8
0.15	5.96	757.7	9.36	404.2	11.57	249.5
	$t_{relax} = 30.0$ ms		$t_{relax} = 21.6$ ms		$t_{relax} = 17.5$ ms	

Table S5. SOAS data for PP-66						
	$T = 180$℃		$T = 200$℃		$T = 220$℃	
Frequency (Hz)	Tan Delta	η (Pa·s)	Tan Delta	η (Pa·s)	Tan Delta	η (Pa·s)
60.0	0.55	213.2	0.64	168.8	0.73	137.0
37.9	0.75	297.7	0.86	230.1	0.98	182.0
23.9	0.88	386.9	1.03	290.6	1.17	225.1
15.1	1.00	489.9	1.18	357.4	1.35	271.4
9.51	1.13	610.3	1.35	431.8	1.55	323.3
6.00	1.27	747.7	1.54	513.9	1.78	377.5
3.79	1.43	901.1	1.77	598.8	2.05	435.1
2.39	1.62	1068.0	2.04	688.9	2.38	493.7
1.51	1.85	1245.0	2.37	775.6	2.79	548.5
0.95	2.11	1427.0	2.78	859.5	3.30	600.1
0.60	2.44	1610.4	3.29	936.1	3.95	646.7
0.38	2.85	1790.1	3.92	1007.0	4.77	688.3
0.24	3.36	1955.9	4.69	1069.4	5.81	720.4
0.15	3.98	2118.0	5.76	1123.2	7.17	750.8
	$t_{relax} = 65.1$ ms		$t_{relax} = 38.4$ ms		$t_{relax} = 27.3$ ms	

Supporting Note 4: Plots for Polypropylene 66

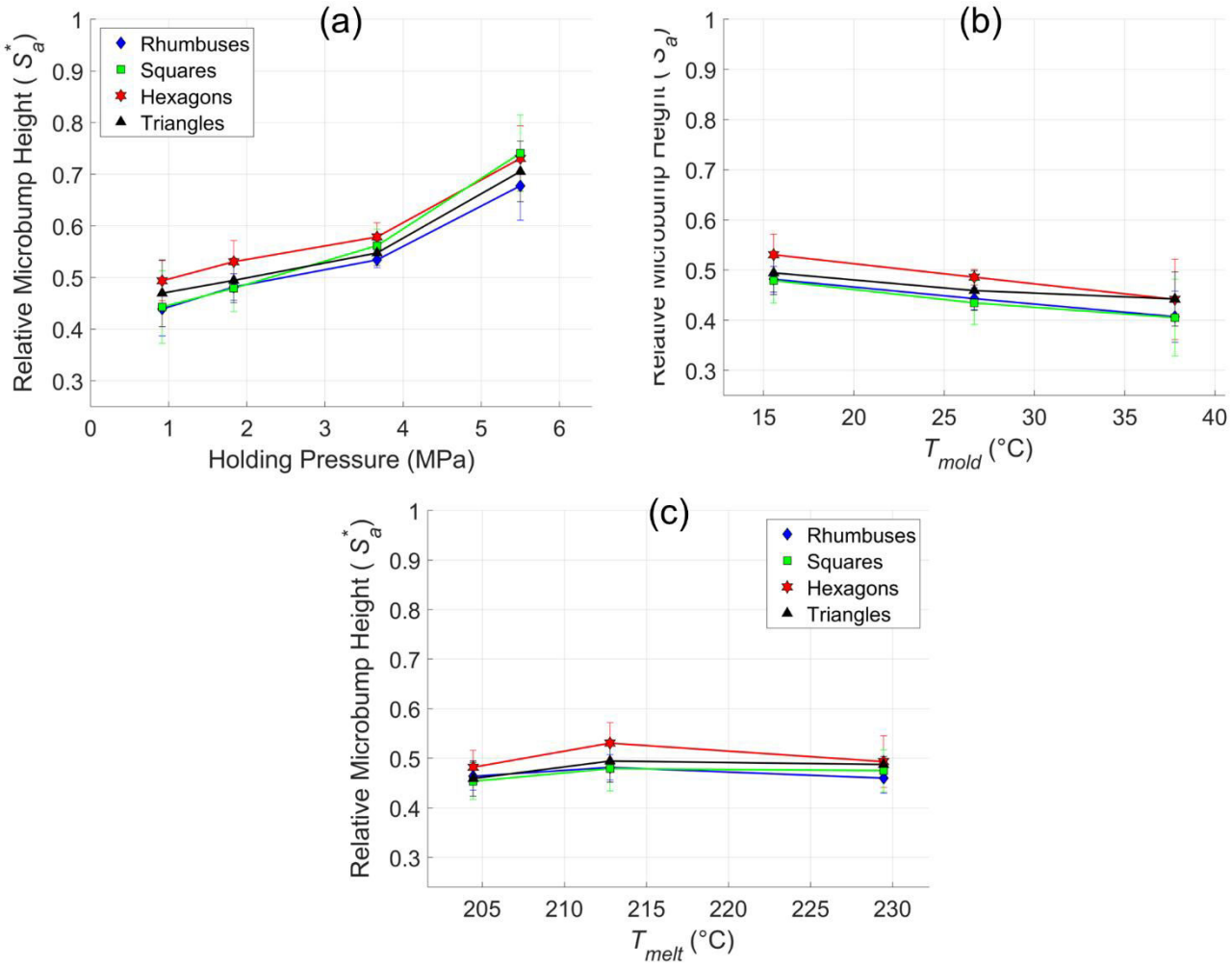

Figure S4. Influence of different injection molding parameters on the molding fidelity for PP-66.